

Electronic Supplementary Information (ESI):

First-Row Transition Metal Dichalcogenide Catalysts for Hydrogen Evolution Reaction

Desheng Kong,^a Judy J. Cha,^a Haotian Wang,^b Hye Ryoung Lee,^c and Yi Cui*^{ad}

^a Department of Materials Science and Engineering, Stanford University, Stanford, CA 94305, USA.
Tel: 1-650-723-4613; E-mail: yicui@stanford.edu

^b Department of Applied Physics, Stanford University, Stanford, CA 94305, USA.

^c Department of Electrical Engineering, Stanford University, Stanford, CA 94305, USA.

^d Stanford Institute for Materials and Energy Sciences, SLAC National Accelerator Laboratory, 2575 Sand Hill Road, Menlo Park, California 94025, USA.

Contents

Experimental Details

Supplementary Figures

- **S1: Active sites of three classes of of hydrogenases**
- **S2: Schematic of the synthesis setup.**
- **S3: Overview SEM images of a CoSe₂ film and a FeS₂ film.**
- **S4: Electron diffraction pattern of a CoSe₂ film acquired in TEM.**
- **S5: Characterizations of CoS₂ films.**
- **S6: Characterizations of NiS₂ films.**
- **S7: Characterizations of NiSe₂ films.**
- **S8: Characterizations of FeS₂ films.**
- **S9: Characterizations of FeSe₂ films.**
- **S10: XPS spectrum of Fe_{0.43}Co_{0.57}S₂ film.**
- **S11: XPS spectrum of Co_{0.56}Ni_{0.44}Se₂ film.**
- **S12: XPS spectrum of Co_{0.32}Ni_{0.68}S₂ film.**
- **S13: Schematic of density-of-states (DOS) of dichalcogenides.**
- **S14: Additional stability tests of transition metal dichalcogenide films.**
- **S15: Compositional analyses of CoSe₂ nanoparticles.**

Supplementary Tables

- **S1: Coordination number of metal atoms on low-index surfaces of FeS₂ with pyrite structure.**
- **S2: Summary of AFM measurements.**
- **S3: Electrochemical measurements of FeS₂ film.**
- **S4: Electrochemical measurements of FeSe₂ film.**
- **S5: Electrochemical measurements of Fe_{0.43}Co_{0.57}S₂ film.**
- **S6: Electrochemical measurements of CoS₂ film.**
- **S7: Electrochemical measurements of CoSe₂ film.**
- **S8: Electrochemical measurements of Co_{0.56}Ni_{0.44}Se₂ film.**
- **S9: Electrochemical measurements of Co_{0.32}Ni_{0.68}S₂ film.**
- **S10: Electrochemical measurements of NiS₂ film.**
- **S11: Electrochemical measurements of NiSe₂ film.**

Experimental Details

Synthesis and Preparation. Transition metal dichalcogenide films are synthesized inside a single-zone, 12-inch horizontal tube furnace (Lindberg/Blue M) equipped with a 1-inch-diameter quartz tube. The synthesis setup is illustrated in Fig. S1. The substrate is initially coated with a thin metal film as a precursor by e-beam evaporation. A 20 nm-thick metal layer is used to grow binary dichalcogenides, whereas a bilayer metal film is used for ternary dichalcogenides (20nm Co/20nm Fe for $\text{Fe}_{0.43}\text{Co}_{0.57}\text{S}_2$, 20nm Co/15 nm Ni for $\text{Co}_{0.56}\text{Ni}_{0.44}\text{Se}_2$ and 20nm Co/50nm Ni for $\text{Co}_{0.32}\text{Ni}_{0.68}\text{S}_2$). The substrate is placed at the hot center of the tube furnace. Sulfur/selenium powder (from Sigma Aldrich) is placed at the upstream side of the furnace at carefully adjusted locations to set the temperature. The tube is pumped to a base pressure of 100 mTorr and flushed with Ar gas several times to remove residual oxygen. Subsequently, the heating center of the furnace is quickly elevated to the reaction temperature of 550 °C for disulfides and 450 °C for diselenides in 20 min, and the sulfur/selenium precursor is kept at ~220/300 °C respectively, well above their melting temperatures. During the synthesis, Ar gas is kept flowing at a rate of 100 sccm to transport sulfur/selenium to the substrate. The furnace is held at the reaction temperature for ~20 to 30 min to fully convert the metal films, followed by natural cool-down. Notice that a cold trap (loaded with dry ice in isopropyl alcohol, from A&N Corporation) is installed on the exhaust gas line to prevent the release of toxic sulfur and selenium vapor during the reaction.

CoSe_2 nanoparticles are grown with a quite similar procedure, where carbon black nanoparticles ($75\text{m}^2/\text{g}$, Alfa Aesar) are used as a template. A slurry of carbon black (8 wt%) and polyvinylpyrrolidone (PVP, 2 wt%) dissolved in ethanol is prepared at room temperature. The slurry is drop casted onto the glassy carbon substrate and dried naturally to form a carbon black nanoparticle assembly weighing $\sim 1.5 \text{ mg/cm}^2$. Subsequently, Co is deposited onto the carbon black nanoparticles by DC sputtering in a ATC Orion Sputtering System (AJA International, Inc.) to yield $\sim 10 \mu\text{g}/\text{cm}^2$ coating. The sputtering is performed by supplying a DC power of 100W for 3 minutes at 5 mTorr pressure with 25 sccm Ar flow. Similar conditions have been used previously to achieve conformal coating for preparing core-shelled CuO/Co nanowires¹. Notice that the Co layer is likely in the form of randomly distributed fine nanoparticles instead of a continuous film over carbon black nanoparticles, due to the short duration of sputtering. Co/CoSe_2 core-shell nanoparticles are then prepared by selenization in the tube furnace. These nanoparticles are binded by calcinated PVP to form agglomerated assembly on glassy carbon substrate, readily used as an electrocatalyst. The mass of active CoSe_2 component is $\sim 37 \mu\text{g}/\text{cm}^2$. The control sample of carbon black is prepared by drop-casting the slurry onto glassy carbon substrate, followed by thermal annealing in the tube furnace at 450 °C for 20 min.

Characterizations. Characterizations were carried out using SEM (FEI Nova NanoSEM 450), TEM (FEI Tecnai G2 F20 X-Twin microscope at 200 keV) equipped with an EDX spectrometer, Raman spectroscopy (WITEC Raman spectrometer), X-ray photoelectron spectroscopy (XPS, SSI S-Probe XPS spectrometer with Al(Kα) source) and atomic force microscopy (AFM, Park Systems XE-70). Films for TEM characterization are prepared on an oxidized silicon substrate (300 nm SiO_2/Si), followed by a lift-off process to transfer the films onto carbon membranes supported on nickel or copper TEM grids by etching away the sacrificial SiO_2 layer in dilute HF solution. AFM data are processed and analyzed byXEI program (Park System Corp.). The Raman spectra, which have a spectral cut-off at $\sim 175 \text{ cm}^{-1}$, are excited by a 531 nm laser with attenuated intensity to avoid local overheating

Electrochemical Measurements. Dichalcogenide films are grown on mirror polished glassy carbon (from HTW Hochtemperatur-Werkstoffe GmbH) to study the activity for HER. Electrochemically inert, hydrophobic wax (Apiezon wax W-W100) is used to define the 1 cm^2 electrode area. A metal alligator clip is used to connect the working electrode with an external circuit. The measurements are performed in 0.5 M H_2SO_4 solution (dearated by N_2) using a three

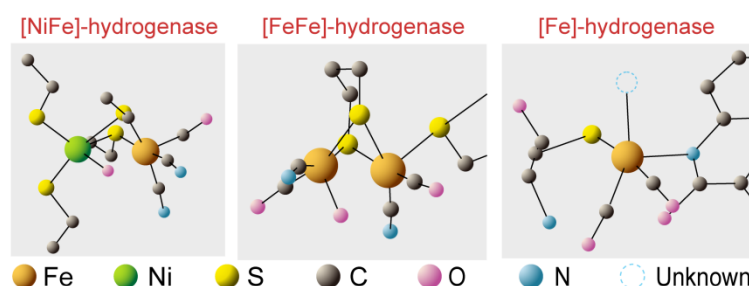
electrode setup, with a saturated calomel reference electrode (SCE, from Accumet), a graphite rod (99.999%, from Sigma Aldrich) counter electrode, and the glassy carbon working electrode. The reference electrode is calibrated in H₂ saturated electrolyte with respect to an *in situ* reverse hydrogen electrode (RHE), by using two platinum wires as working and counter electrodes, which yields the relation $E(\text{RHE}) = E(\text{SCE}) + 0.279$ V. The saturation condition is confirmed by minimizing the potential difference between the working and counter electrodes to less than a few mV. Linear sweep voltammetry (scan rate of 2 mV/s) and AC impedance spectroscopy (at zero overpotential) are recorded using a Biologic VSP potentiostat. For a Tafel plot, the linear portion at low overpotential is fit to the Tafel equation. Within the low overpotential range, the fit is not affected by the evolution of hydrogen bubbles or other kinetic effects. All data have been corrected for a small ohmic drop (<4 Ω) based on impedance spectroscopy.

The long-term stability is assessed by taking continuous cyclic voltammograms at an accelerated scanning rate of 50 mV/s for 1000 times. These cyclic voltammograms are carried out between 0.1 V and a low potential limit that drives a large current density of -10 mA/cm². The polarization curves before and after cycling are recorded under quasi-equilibrium conditions at a slower scan rate of 2 mV/s.

Commercial platinum wire (Accumet Model 13-620-115) is measured to establish a reference point of state-of-art HER catalyst. The experimental conditions are the same as for dichalcogenide catalysts, except that another platinum wire is used as counter electrode.

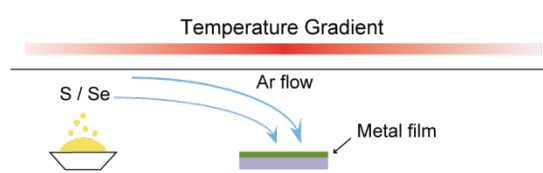
Supplementary Figures

Figure S1. Active sites of three classes of hydrogenases.



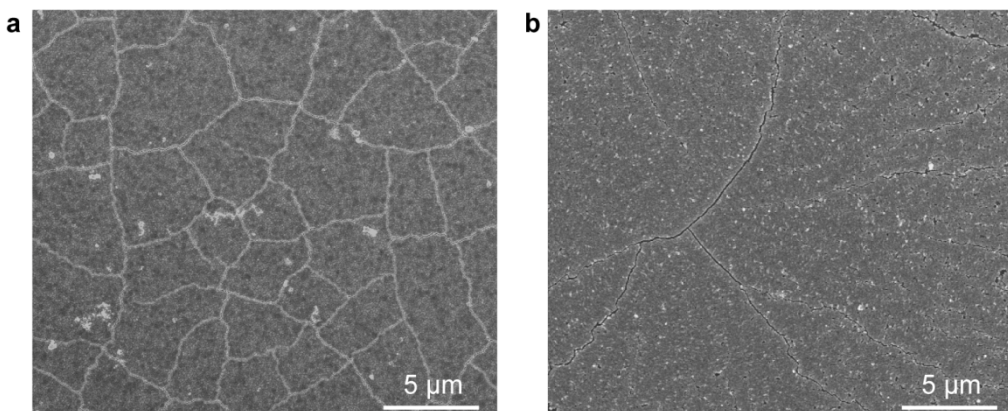
The active site structure of [NiFe]-hydrogenase (left), [FeFe]-hydrogenase (middle), and [Fe]-hydrogenase (right), sharing a low-spin Fe (II) with five ligands in a octahedral ligand field, exemplifying the remarkable convergent evolution^{2,3}. A Fe center in such square pyramidal environment is well suited to bind with adsorbates at the vacant sixth coordination site. The structure of the active center provides inspirations to search for active heterogeneous catalysts in inorganic solids. Notice that the basic structure of these active centers does not fully describe the remarkable activity of hydrogenases. The catalytic activity is also largely affected by the ligand compositions and associated delicate electronic structure.

Figure S2. Schematic of the synthesis setup.



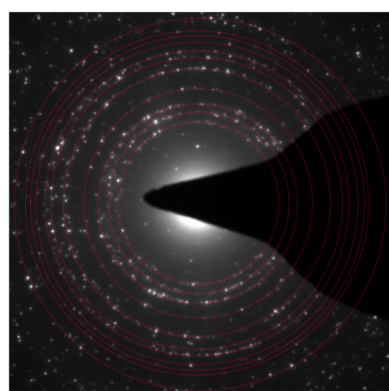
Transition metal dichalcogenide films are synthesized in a 12-inch horizontal tube furnace (Lindberg/Blue M) equipped with a 1-inch-diameter quartz tube. The substrate is initially coated with a thin metal film as the precursor by e-beam evaporation. Sulfur/selenium powder is placed at the upstream for subsequent sulfurization/selenization. During the synthesis, the substrate is located at the heating center of the furnace, with flowing Ar to transport sulfur/selenium vapor to convert the metal precursor into the corresponding dichalcogenides.

Figure S3. Overview SEM images of a CoSe₂ film and a FeS₂ film.



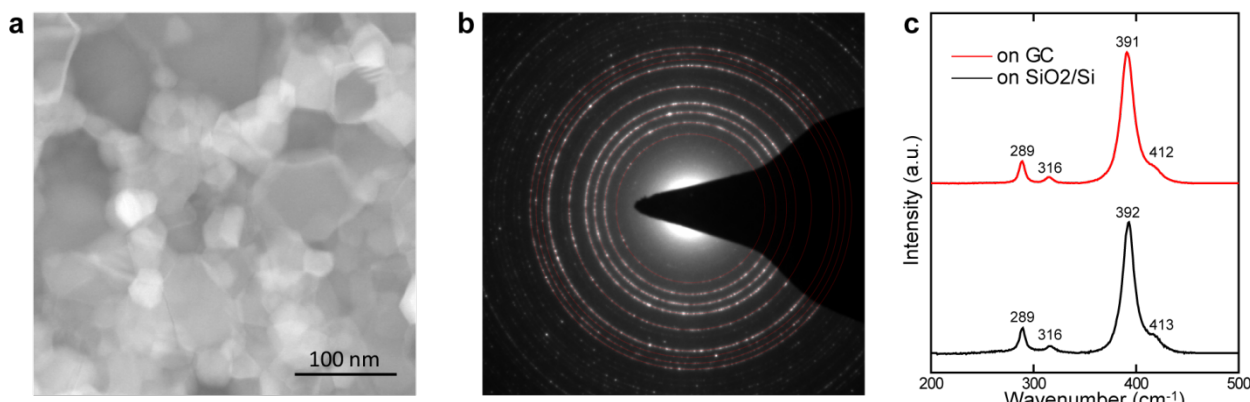
The overview SEM images of representative transition metal dichalcogenide films reveal the morphology of as-grown films. **a**, SEM image of a CoSe₂ film grown on glassy carbon substrate showing the film is fairly uniform and flat. In addition, small cracks are also present across the entire film. **b**, SEM image of a FeS₂ film grown on glassy carbon substrate.

Figure S4. Electron diffraction pattern of a CoSe₂ film acquired in TEM.



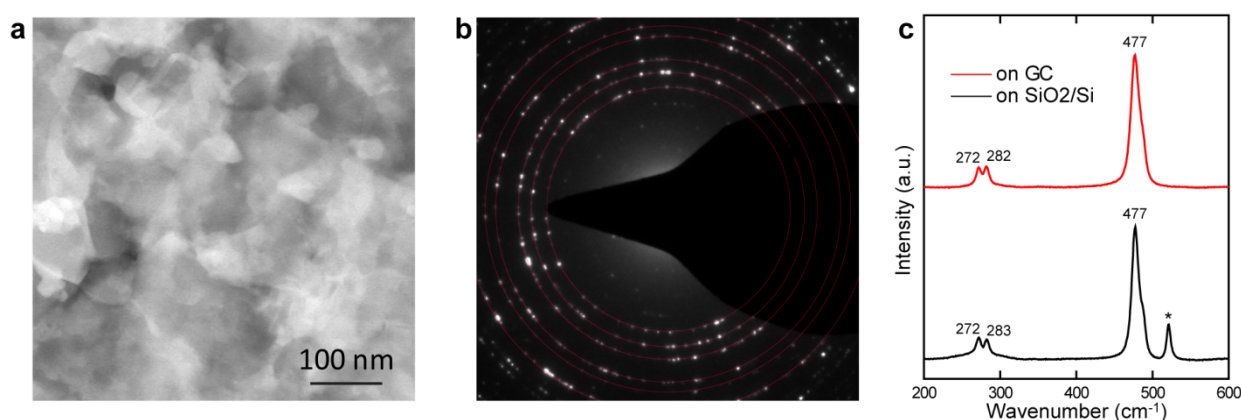
The ring pattern confirms the polycrystalline nature of the film with the red rings to guide the eye. The diffraction rings are consistent with the CoSe₂ phase with pyrite crystal structure. The lattice parameter is $a = 5.85 \text{ \AA}$ by fitting the diffraction pattern, matching the bulk value of 5.859 \AA (PDF#04-003-1990).

Figure S5. Characterizations of CoS₂ films.



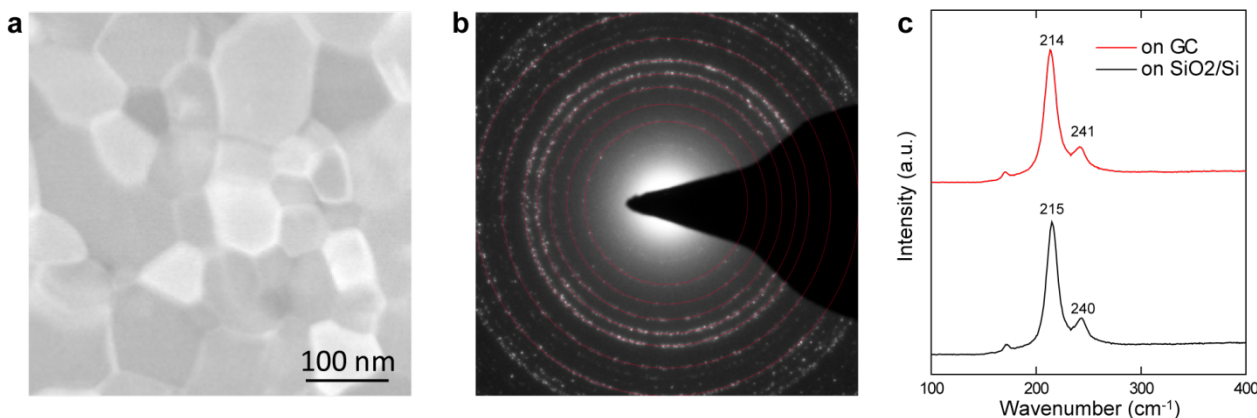
a, Dark field (DF) - scanning transmission electron microscopy (STEM) image of a typical CoS₂ film, revealing the granular nature of the film. The less intensity found in larger grains are due to the intensity turn over for these thicker grains. **b**, Electron diffraction pattern of a CoS₂ film acquired in TEM, showing the ring pattern of the polycrystalline film. The diffraction pattern, in which the red circles are shown to guide the eye, well matches the CoS₂ phase with pyrite structure. The lattice parameter is $a = 5.53 \text{ \AA}$ by fitting the diffraction pattern, consistent with the bulk value of 5.538 \AA (PDF#00-041-1471). **c**, Raman spectra from CoS₂ films grown on glassy carbon (GC) and oxidized silicon (300 nm SiO₂/Si) substrates, respectively. The peaks at 289, 316, 391 and 412 cm^{-1} correspond to the characteristic active modes of CoS₂ with pyrite structure^{4,5}.

Figure S6. Characterizations of NiS₂ films.



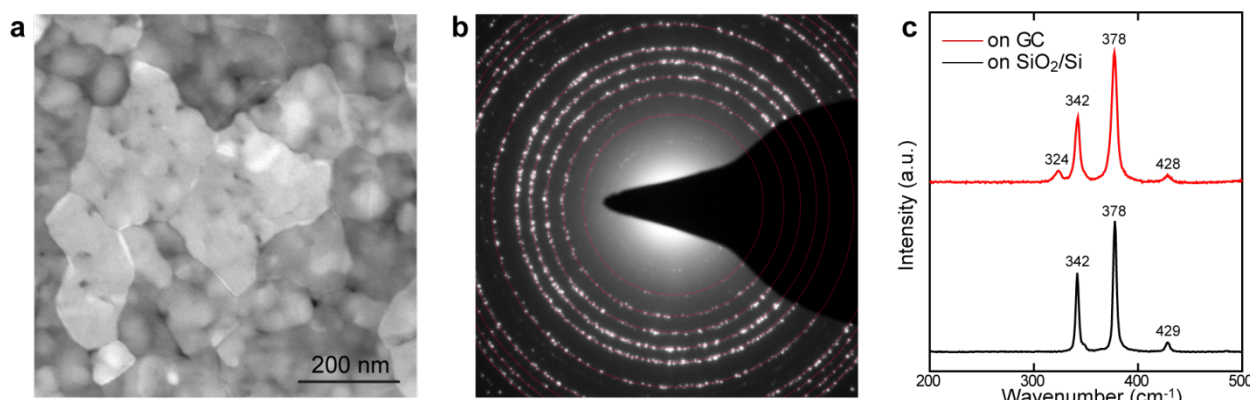
a, DF-STEM image of a typical NiS₂ film, revealing the polycrystalline structure of the film. **b**, Electron diffraction pattern of a NiS₂ film acquired in TEM, showing the ring pattern of the polycrystalline film. The diffraction pattern, in which the red circles are shown to guide the eye, well matches the NiS₂ phase with pyrite structure. The lattice parameter is $a = 5.67 \text{ \AA}$ by fitting the diffraction pattern, consistent with the bulk value of 5.677 \AA (PDF#04-004-4343). **c**, Raman spectra from NiS₂ films grown on glassy carbon (GC) and oxidized silicon (300 nm SiO₂/Si) substrates, respectively. The peaks at 272, 283 and 477 cm^{-1} correspond to the characteristic active modes of NiS₂ with pyrite structure⁴⁻⁷. For NiS₂ film grown on oxidized silicon, the peak at 520 cm^{-1} marked by the star comes from the silicon substrate underneath⁸.

Figure S7. Characterizations of NiSe₂ films.



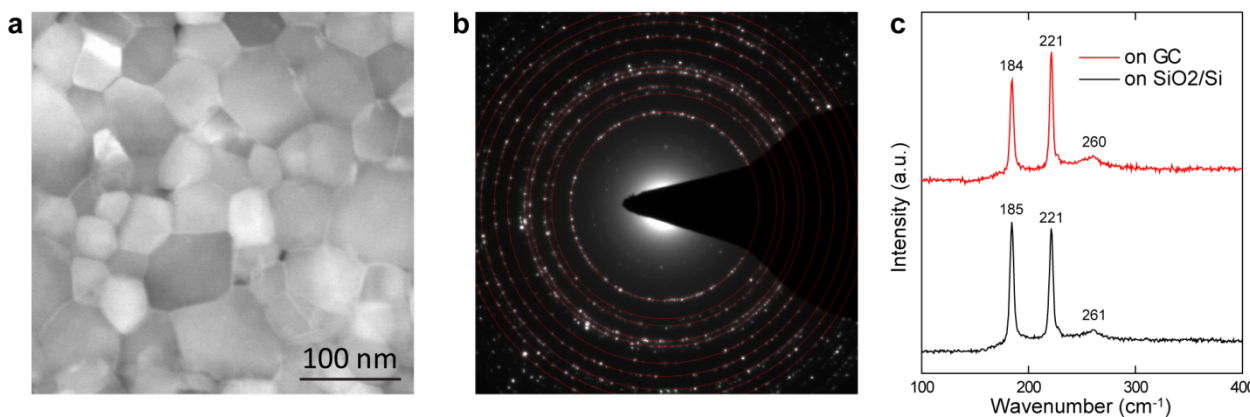
a, DF-STEM image of a typical NiSe₂ film, revealing the polycrystalline structure of the film. **b**, Electron diffraction pattern of a NiSe₂ film acquired in TEM, showing ring pattern of the polycrystalline film. The diffraction pattern, in which the red circles are shown to guide the eye, well matches the NiS₂ phase with pyrite structure. The lattice parameter is $a = 6.00 \text{ \AA}$ by fitting the diffraction pattern, consistent with the bulk value of 5.991 \AA (PDF#00-041-1495). **c**, Raman spectra from NiSe₂ films grown on glassy carbon (GC) and oxidized silicon (300 nm SiO₂/Si) substrates, respectively. The peaks at 214 and 240 cm^{-1} correspond to the characteristic active modes of NiSe₂ with pyrite structure⁶.

Figure S8. Characterizations of FeS₂ films.



a, DF-STEM image of a typical FeS₂ film, revealing the polycrystalline structure of the film. **b**, Electron diffraction pattern of a FeS₂ film acquired in TEM, showing ring pattern of the polycrystalline film. The diffraction pattern, in which the red rings are shown to guide the eye, well matches the FeS₂ phase with pyrite structure. The lattice parameter is $a = 5.42 \text{ \AA}$ by fitting the diffraction pattern, consistent with the bulk value of 5.418 \AA (PDF#00-042-1340). **c**, Raman spectra from FeS₂ films grown on glassy carbon (GC) and oxidized silicon (300 nm SiO₂/Si) substrates, respectively. The peaks at 342, 378 and 429 cm^{-1} correspond to the characteristic active modes of FeS₂ with pyrite structure⁹⁻¹¹, whereas the peak at 324 cm^{-1} corresponds to the characteristic mode of FeS₂ with marcasite structure¹². It is not surprising to observe the coexistence of both phases in a polycrystalline film as they share many structural similarities. The metal cations are octahedrally coordinated in both crystals. The lattice parameters of FeS₂ in marcasite phase are $a = 4.443 \text{ \AA}$, $b = 5.425 \text{ \AA}$, and $c = 3.387 \text{ \AA}$ (PDF#04-003-2016). The b value and [101] ($(a^2+c^2)^{1/2} = 5.587 \text{ \AA}$) are close to the lattice parameter of FeS₂ in pyrite phase with small lattice mismatches of 0.1% and 3% respectively, which is the basis for epitaxial growth^{11, 13}. The subtle structural distinction is mainly associated with the octahedral linkage. The octahedra are corner-shared in pyrite and edge-shared in marcasite (see Fig. 1b and 1c). Accordingly, the epitaxial growth of marcasite on pyrite has also been widely observed in experiments¹⁴.

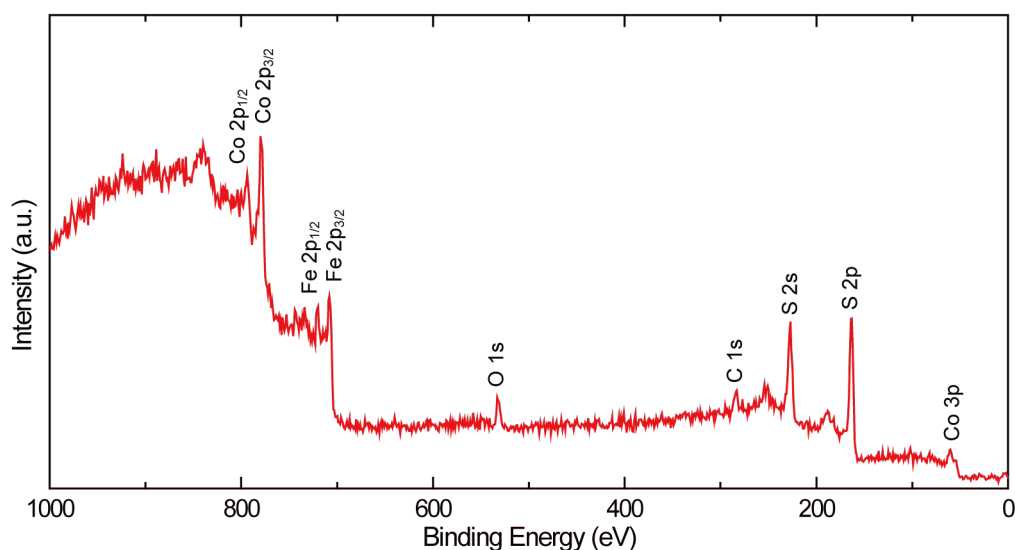
Figure S9. Characterizations of FeSe₂ films.



a, DF-STEM image of a typical FeSe₂ film, revealing the polycrystalline structure of the film. **b**, Electron diffraction pattern of a FeSe₂ film acquired in TEM, showing ring pattern of the polycrystalline film. The

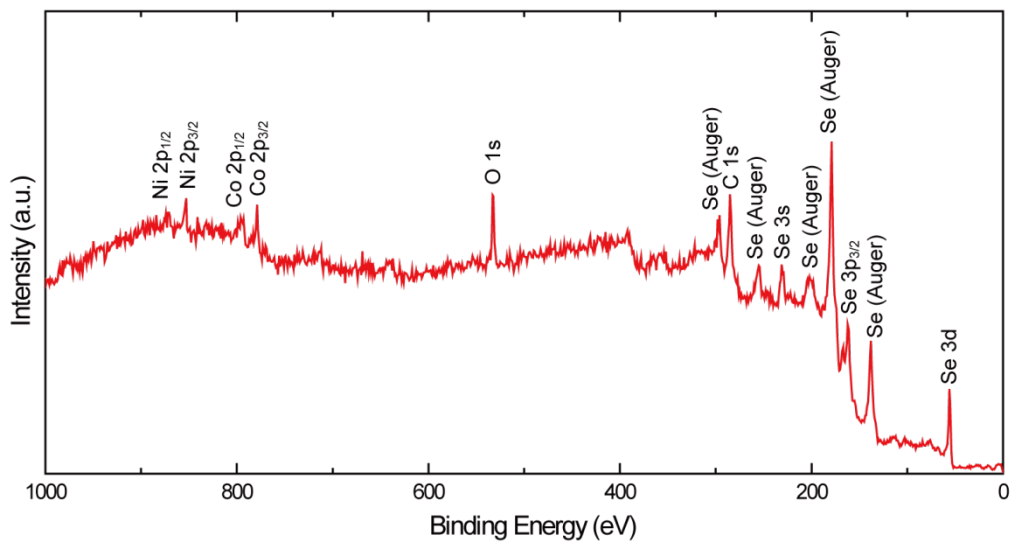
diffraction pattern, in which the red rings are shown to guide the eye, well matches the FeSe_2 phase with macarsite structure. The lattice parameters are $a = 4.80 \text{ \AA}$, $b = 5.81 \text{ \AA}$, and $c = 3.58 \text{ \AA}$ by fitting the diffraction pattern, close to the bulk values $a = 4.804 \text{ \AA}$, $b = 5.784 \text{ \AA}$, and $c = 3.586 \text{ \AA}$ (PDF#04-003-1738). The result is consistent with the previous studies on selenization of pre-deposited Fe films that yields FeSe_2 with marcasite structure¹⁵. **c**, Raman spectra from FeSe_2 films grown on glassy carbon (GC) and oxidized silicon (300 nm SiO_2/Si) substrates, respectively. The peaks at 185, 221 and 260 cm^{-1} correspond to the characterisitic active modes of FeSe_2 with macarsite structure¹².

Figure S10. XPS spectrum of $\text{Fe}_{0.43}\text{Co}_{0.57}\text{S}_2$ film.



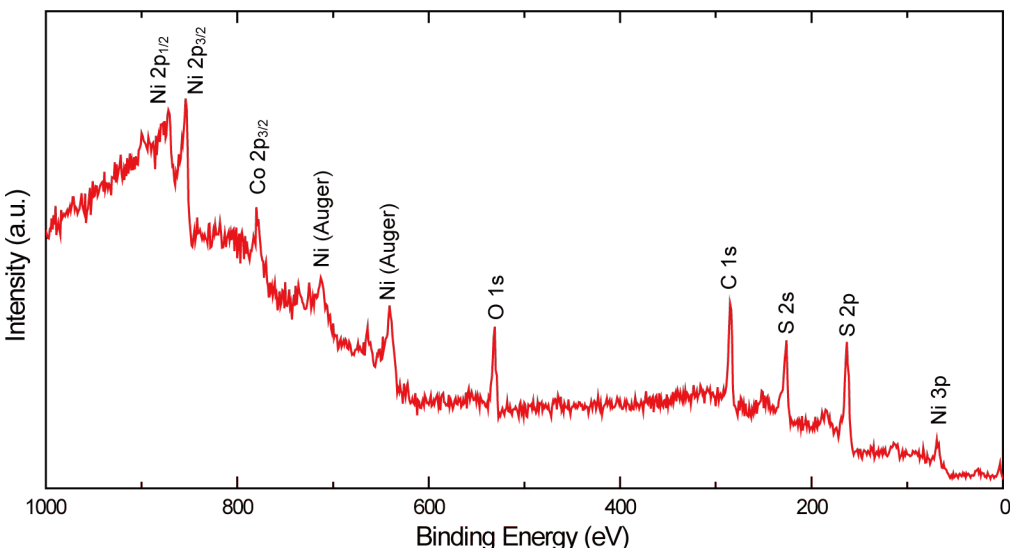
The film is formed by sulfurizing a Co/Fe (20 nm/20 nm) double-layer film deposited sequentially by e-beam evaporation. During the synthesis, the metal precursors are mixed and sulfurized to form the ternary disulfide. XPS spectrum reveals the atomic ratio of $\text{Fe}/\text{Co} \sim 0.7393$, which corresponds to the surface chemical composition as $\text{Fe}_{0.43}\text{Co}_{0.57}\text{S}_2$.

Figure S11. XPS spectrum of $\text{Co}_{0.56}\text{Ni}_{0.44}\text{Se}_2$ film.



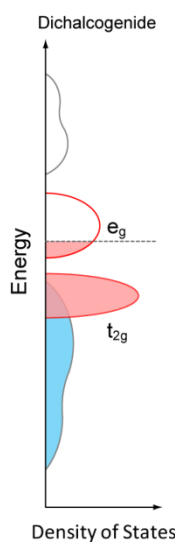
The film is formed by selenizing a Co/Ni (20 nm/15nm) double-layer film deposited sequentially by e-beam evaporation. During the synthesis, the metal precursors are mixed and selenized to form the ternary diselenide. XPS spectrum reveals the atomic ratio of Co/Ni ~ 1.297 , which corresponds to the surface chemical composition as $\text{Co}_{0.56}\text{Ni}_{0.44}\text{Se}_2$.

Figure S12. XPS spectrum of $\text{Co}_{0.32}\text{Ni}_{0.68}\text{S}_2$ film.



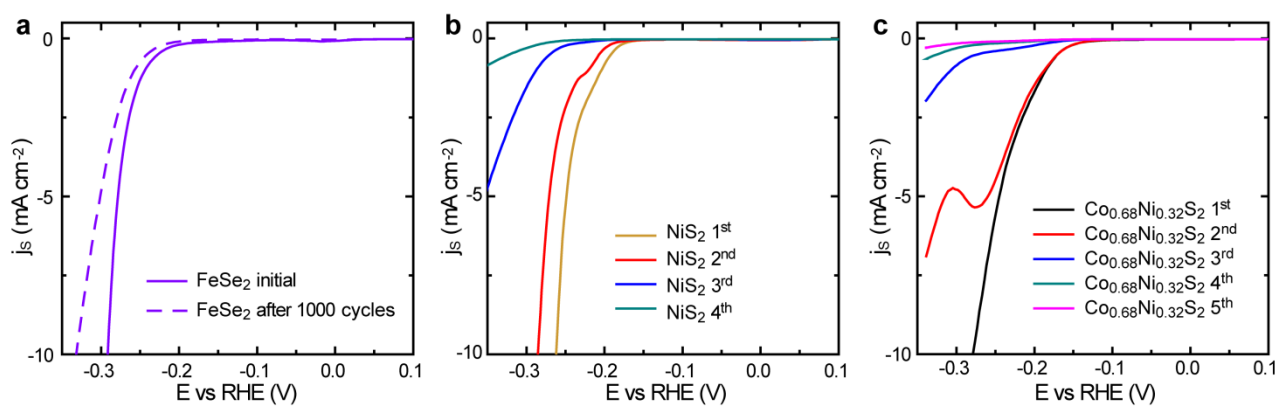
The film is formed by sulfurizing a Co/Ni (20 nm/50nm) double-layer film deposited sequentially by e-beam evaporation. During the synthesis, the metal precursors are mixed and sulfurized to form the ternary disulfide. XPS spectrum reveals the atomic ratio of Co/Ni ~ 0.4662 , which corresponds to the surface chemical composition as $\text{Co}_{0.32}\text{Ni}_{0.68}\text{S}_2$.

Figure S13. Schematic of density-of-states (DOS) of dichalcogenides.



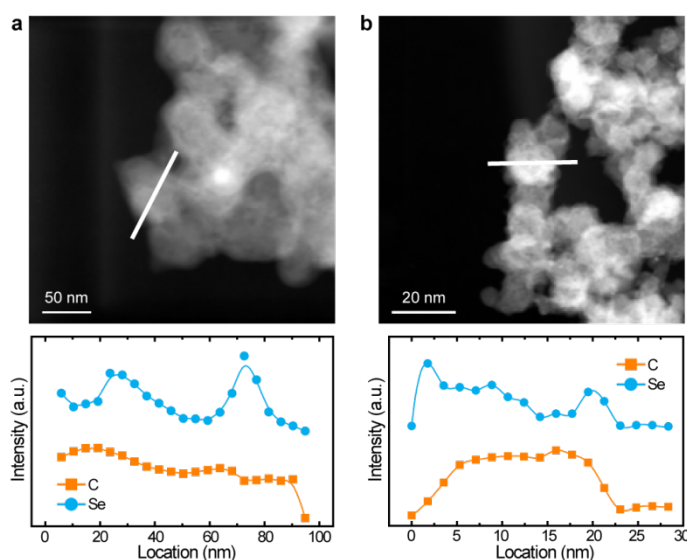
DOS of CoS_2 is shown as an example¹⁶. Notice that these dichalcogenides are controlled by short range interactions to yield similar band structures, where the chemical potential varies with the occupancy of the d electrons in the e_g band^{17, 18}. For inorganic electrocatalysts, the electronic states near Fermi level are responsible for the adsorption strength of reactants^{19, 20}. Partially filled e_g bands are likely the optimal conditions for high HER activity.

Figure S14. Additional stability tests of transition metal dichalcogenide films.



a, Polarization curves of FeSe_2 before and after 1000 potential cycles. Apparently, certain degradation in HER activity is observed on FeSe_2 film after long-term cycling. **b**, Polarization curves of NiS_2 for the initial several potential sweeps. The decrease of HER activty from sweep to sweep is likely due to the peeling off NiS_2 film from the glassy carbon substrate. **c**, Polarzation curves of $\text{Co}_{0.68}\text{Ni}_{0.32}\text{S}_2$ for the initial several potential sweeps, showing degradation of HER activity from sweep to sweep.

Figure S15. Compositional analyses of CoSe₂ nanoparticles.



a,b, Dark-field STEM images of CoSe₂ nanoparticle assembly (top). EDX elemental line scans of a nanoparticle corresponding to the white lines in the STEM images (bottom). Generally, the elemental line scans show Se is present throughout the nanostructure with increased intensity at the particle edges, whereas C is evenly distributed. The measurements reveal C and CoSe₂ are roughly distributed in a core-shell structure. However, the elemental distribution is not entirely symmetric, suggesting certain inhomogeneity of the CoSe₂ layer over carbon black nanoparticle.

Supplementary Tables

Table S1. Coordination number for metal cations on low-index surfaces of FeS₂ with pyrite structure.

Miller Index	Surface Metal Coordination
(100)	5
(110)	4
(110), defective	4 and 5
(210)	4 and 5
(111)	5 and 6

The results are based on computational studies on FeS₂^{13, 21, 22}. On all low-index surfaces, some surface Fe sites are reduced from saturated sixfold coordination to generate a non-polar termination with low surface energy¹³. The tendency to lower the surface metal site coordination for a non-polar surface is expected to occur in other dichalcogenides.

Table S2. Summary of AFM measurements.

	Roughness (nm)	Surface Area / Geometric Area
FeS ₂	9.5	1.039
FeSe ₂	11.5	1.057
Fe _{0.43} Co _{0.57} S ₂	50.0	1.059
CoS ₂	68.3	1.082
CoSe ₂	8.8	1.020
Co _{0.56} Ni _{0.44} Se ₂	88.6	1.070
Co _{0.32} Ni _{0.68} S ₂	10.1	1.038
NiS ₂	47.2	1.075
NiSe ₂	65.2	1.127

AFM topographic measurements are performed on dichalcogenide films grown on glassy carbon electrodes. The surface topology is acquired from multiple samples to yield averaged surface parameters. The roughness and specific surface area are calculated by XEI program (from Park Systems Corp).

Table S3. Electrochemical measurements of FeS₂ film.

FeS ₂		
	Tafel Slope (mV/dec.)	j ₀ (A cm ⁻²)
Sample 1	67.8	7.2e-7
Sample 2	62.5	5.2e-7
Sample 3	65.8	6.9e-7
Sample 4	77.2	1.7e-6

Table S4. Electrochemical measurements of FeSe₂ film.

FeSe ₂		
	Tafel Slope (mV/dec.)	j ₀ (A cm ⁻²)
Sample 1	66.3	2.7e-7
Sample 2	65.3	3.0e-7
Sample 3	71.6	4.6e-7
Sample 4	62.1	4.7e-7

Table S5. Electrochemical measurements of $\text{Fe}_{0.43}\text{Co}_{0.57}\text{S}_2$ film.

Fe _{0.43} Co _{0.57} S ₂		
	Tafel Slope (mV/dec.)	j ₀ (A cm ⁻²)
Sample 1	55.4	1.6e-7
Sample 2	55.9	1.6e-6
Sample 3	64.4	1.6e-6
Sample 4	60.8	1.3e-6

Table S6. Electrochemical measurements of CoS₂ film.

CoS ₂		
	Tafel Slope(mV/dec.)	j ₀ (A cm ⁻²)
Sample 1	46.6	7.0e-8
Sample 2	44.6	5.4e-8
Sample 3	46.3	6.9e-8
Sample 4	43.7	6.3e-8

Table S7. Electrochemical measurements of CoSe₂ film.

CoSe ₂		
	Tafel Slope (mV/dec.)	j ₀ (A cm ⁻²)
Sample 1	40.8	4.1e-8
Sample 2	43.0	8.5e-8
Sample 3	42.4	7.5e-8
Sample 4	42.5	5.0e-8

Table S8. Electrochemical measurements of $\text{Co}_{0.56}\text{Ni}_{0.44}\text{Se}_2$ film.

Co _{0.56} Ni _{0.44} Se ₂		
	Tafel Slope (mV/dec.)	j ₀ (A cm ⁻²)
Sample 1	50.5	5.6e-8
Sample 2	49.7	7.1e-8
Sample 3	54.7	1.0e-7
Sample 4	45.6	4.2e-8

Table S9. Electrochemical measurements of Co_{0.32}Ni_{0.68}S₂ film.

Co _{0.32} Ni _{0.68} S ₂		
	Tafel Slope (mV/dec.)	j ₀ (A cm ⁻²)
Sample 1	66.8	3.0e-7
Sample 2	63.9	2.1e-7
Sample 3	66.9	3.2e-7
Sample 4	66.3	2.5e-7

Table S10. Electrochemical measurements of NiS₂ film.

NiS ₂		
	Tafel Slope (mV/dec.)	j ₀ (A cm ⁻²)
Sample 1	43.7	1.9e-8
Sample 2	45.6	2.1e-8
Sample 3	44.9	1.3e-8
Sample 4	41.6	1.4e-8

Table S11. Electrochemical measurements of NiSe₂ film.

NiSe ₂		
	Tafel Slope (mV/dec.)	j ₀ (A cm ⁻²)
Sample 1	56.4	5.7e-7
Sample 2	56.9	7.5e-7
Sample 3	56.6	8.3e-7
Sample 4	62.0	5.8e-7

REFERENCES

1. W. Shi and N. Chopra, *ACS Appl. Mater. Interfaces*, 2012, **4**, 5590-5607.
2. S. Shima, O. Pilak, S. Vogt, M. Schick, M. S. Stagni, W. Meyer-Klaucke, E. Warkentin, R. K. Thauer and U. Ermler, *Science*, 2008, **321**, 572-575.
3. Y. Nicolet, C. Piras, P. Legrand, C. E. Hatchikian and J. C. Fontecilla-Camps, *Structure*, 1999, **7**, 13-23.
4. E. Anastassakis and C. H. Perry, *J. Chem. Phys.*, 1976, **64**, 3604-3609.

5. L. Zhu, D. Susac, M. Teo, K. C. Wong, P. C. Wong, R. R. Parsons, D. Bizzotto, K. A. R. Mitchell and S. A. Campbell, *J. Catal.*, 2008, **258**, 235-242.
6. C. de las Heras and F. Agulló-Rueda, *J. Phys.: Condens. Matter*, 2000, **12**, 5317.
7. T. Suzuki, K. Uchinokura, T. Sekine and E. Matsuura, *Solid State Commun.*, 1977, **23**, 847-852.
8. J. H. Parker, Jr., D. W. Feldman and M. Ashkin, *Phys. Rev.*, 1967, **155**, 712-714.
9. H. Vogt, T. Chattopadhyay and H. J. Stoltz, *J. Phys. Chem. Solids*, 1983, **44**, 869-873.
10. A. K. Kleppe and A. P. Jephcoat, *Mineral. Mag.*, 2004, **68**, 433-441.
11. M. Cabán-Acevedo, M. S. Faber, Y. Tan, R. J. Hamers and S. Jin, *Nano Lett.*, 2012, **12**, 1977-1982.
12. H. D. Lutz and B. Muller, *Phys. Chem. Miner.*, 1991, **18**, 265-268.
13. R. Sun, M. K. Y. Chan and G. Ceder, *Phys. Rev. B*, 2011, **83**, 235311.
14. D. M. Schleich and H. S. W. Chang, *J. Cryst. Growth*, 1991, **112**, 737-744.
15. N. Hamdadou, A. Khelil, M. Morsli and J. C. Bernåde, *Vacuum*, 2005, **77**, 151-156.
16. S. Ogawa, *J. Appl. Phys.*, 1979, **50**, 2308-2311.
17. J. B. Goodenough, *J. Solid State Chem.*, 1972, **5**, 144-152.
18. P. Raybaud, J. Hafner, G. Kresse and H. Toulhoat, *J. Phys.: Condens. Matter*, 1997, **9**, 11107.
19. J. K. Nørskov, F. Abild-Pedersen, F. Studt and T. Bligaard, *Proc. Natl. Acad. Sci.*, 2011, **108**, 937-943.
20. A. Vojvodic and J. K. Nørskov, *Science*, 2011, **334**, 1355-1356.
21. A. Hung, J. Muscat, I. Yarovsky and S. P. Russo, *Surf. Sci.*, 2002, **513**, 511-524.
22. A. Hung, J. Muscat, I. Yarovsky and S. P. Russo, *Surf. Sci.*, 2002, **520**, 111-119.